

Sub-femtosecond tracing of molecular dynamics during strong-field interaction

Václav Hanus,^{1,*} Sarayoo Kangaparambil,¹ Seyedreza Larimian,¹ Martin Dörner-Kirchner,¹ Xinhua Xie (谢新华),^{1,2} Markus S. Schöffler,³ Gerhard G. Paulus,⁴ Andrius Baltuška,¹ André Staudte,^{5,†} and Markus Kitzler-Zeiler^{1,‡}

¹Photonics Institute, Technische Universität Wien, 1040 Vienna, Austria, EU

²SwissFEL, Paul Scherrer Institute, 5232 Villigen PSI, Switzerland

³Institut für Kernphysik, Goethe-Universität Frankfurt, 60438 Frankfurt, Germany, EU

⁴Institute for Optics and Quantum Electronics, Friedrich-Schiller-Universität Jena, 07743 Jena, Germany, EU

⁵Joint Laboratory for Attosecond Science of the National Research Council and the University of Ottawa, Ottawa, Ontario K1A 0R6, Canada

We introduce and experimentally demonstrate a method, where the two intrinsic time scales of a molecule, the slow nuclear motion and the fast electronic motion, are simultaneously measured in a photo-electron photo-ion coincidence experiment. In our experiment, elliptically polarized, 750 nm, 4.5 fs laser pulses were focused to an intensity of $9 \times 10^{14} \text{W/cm}^2$ onto H_2 . Using coincidence imaging, we directly observe the nuclear wavepacket evolving on the $1s\sigma_g$ state of H_2^+ during its first roundtrip with attosecond temporal and picometer spatial resolution. The demonstrated method should enable insight into the first few femtoseconds of the vibronic dynamics of ionization-induced unimolecular reactions of larger molecules.

Molecular fragmentation and isomerization processes are of fundamental importance in nature. These nuclear rearrangement processes are initiated and ultimately determined by electronic dynamics that can be influenced by precisely timed distortions of the electronic structure with the electric field of strong, ultrashort laser pulses [1–4]. For example, fine variations of the delay between successive ionization events can determine the number of moieties produced during fragmentation of polyatomic molecules [5]. To reveal the dynamics underlying these processes, it is necessary to apply probing techniques that are sensitive to both, the fast electronic dynamics that may take place on attosecond time scales and the slower nuclear motion taking place on the femtosecond time scale. While even the fastest vibrational wavepacket in H_2^+ has been probed successfully shortly *after* its creation using a pump-probe scheme with near-single-cycle pulses [6, 7], it is, however, a major obstacle to trace the molecular dynamics *during* the first few femtoseconds of the interaction of a molecule with a strong laser pulse.

In this Letter, we introduce and experimentally demonstrate a method that is capable of tracing simultaneously electronic and vibrational wavepacket dynamics in a fragmenting molecule on sub-femtosecond times. The method combines the sub-cycle sensitivity inherent to angular streaking that has been applied to studying ionization dynamics in atoms [8–12] and molecules [13–16], with the high structural sensitivity of Coulomb explosion imaging [17–21] to resolve vibrational motion. Our work is inspired by earlier attempts [22] of constructing such a method that has been called *The Molecular Clock*.

We investigate the applicability of this concept by tracing the nuclear and electronic dynamics in H_2^+ triggered by the emission of an electron over several femtoseconds. Upon ionization of H_2^+ various scenarios can take place [23]. The simplest one is that a vibrational wavepacket

is created on the $1s\sigma_g$ energy level following the Franck-Condon (FC) principle [24], see Fig. 1(a). Even for this simplest of all cases it has been shown that the very fast nuclear motion taking place during the ionization event can lead to deviations from the population distribution of vibrational states predicted by the FC principle [25]. In another scenario, shake-up excitations can lead to the population of vibrational states not only on the $1s\sigma_g$ but also on the $2p\sigma_u$ level [26]. In recent photoelectron holography measurements evidence for subcycle population transfer to $2p\sigma_u$ was found [27]. As the vibrational dynamics proceeds after ionization in the presence of the strong laser field, three- or five-photon resonant excitations, can lead to partial population transfer between the $1s\sigma_g$ and $2p\sigma_u$ levels [1, 2]. We show that we can achieve temporal and spatial resolutions of a few tens of attoseconds and about 1 pm – sufficient to disentangle these different scenarios.

To obtain attosecond temporal resolution we employ angular streaking [8, 9] illustrated in Fig. 1(b). Angular streaking exploits the direct mapping of electron momentum to the instantaneous laser electric field at the time of ionization. In elliptically polarized light the electric field vector $\mathbf{E}(t)$ completes a full rotation within one period of the field, $T = 2\pi/\omega$, where ω is the frequency of the light. This rotation serves as the minute hand of a clock: The ionization phase within a laser cycle $\varphi = \omega t_i$ is mapped into the emission angle of the photoelectron via the relation $\mathbf{p}_e = -\mathbf{A}(t_i)$, valid within the strong-field approximation [28, 29], where the laser vector potential $\mathbf{A}(t)$ is connected to the laser electric field by $\mathbf{A}(t) = -\int_{-\infty}^t \mathbf{E}(t') dt'$. Thus, measurement of the electron emission angle in the laboratory frame determines the ionization time t_i within one cycle. In addition, the magnitude of the emitted electron’s momentum vector $|\mathbf{p}_e|$ is proportional to the instantaneous field strength and thereby provides a measure about the ionization time

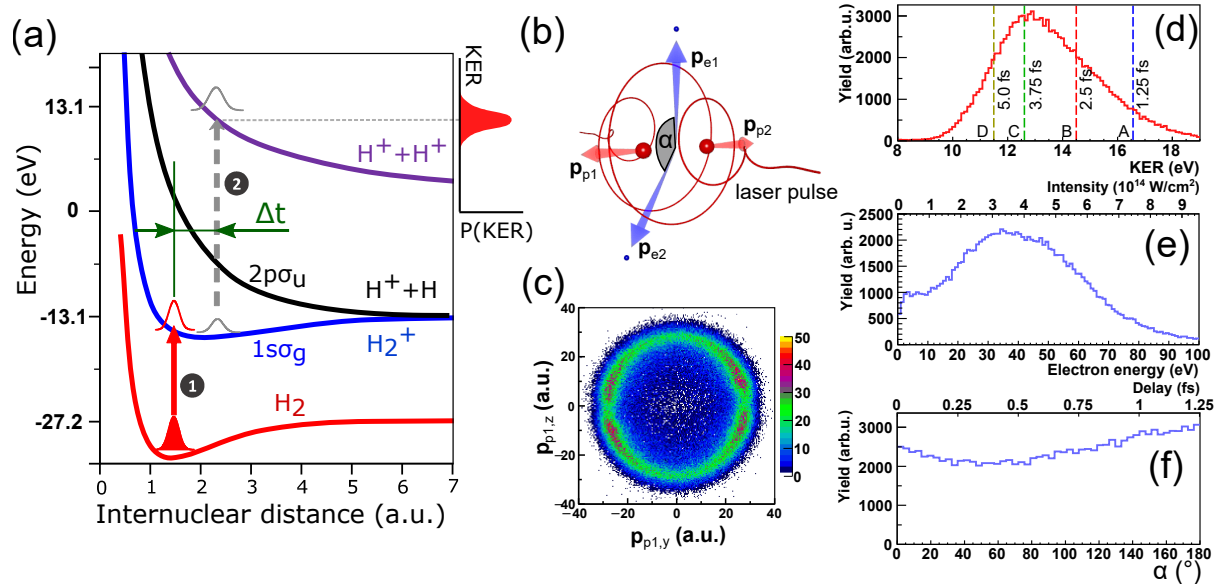


FIG. 1. (a) Schematics of the relevant potential energy surfaces of H_2 . Indicated by arrows are the two ionization steps (1 and 2) that are delayed with respect to each other by Δt . (b) Cartoon of the electron and ion momentum vectors after double ionization of H_2 in an intense elliptically polarized few-cycle laser pulse. (c) Distribution of the proton momentum from intra-pulse double ionization in the polarization plane. The histogram is filled with two detected protons which satisfy a center-of-mass momentum < 10 a.u. The minimum around $p_{p1,z} = 0$ a.u. is due to the dead time of the detector. (d) Kinetic energy release (KER). The lines A-D label certain values of Δt . (e) Photoelectron energy distribution. Upper axis: corresponding laser intensity. (f) Relative emission angle between the two photoelectrons. Upper axis: corresponding ionization delay on a sub-cycle scale.

within the pulse envelope [10].

The hand of the clock on the vibronic time scale is the kinetic energy release (KER) of the protons following double ionization. It has been shown that the kinetic energy released during Coulomb explosion of a molecule into two ionic fragments is a sensitive measure of the distance R where the repulsive Coulombic potential is populated [17, 20, 30–32]. In H_2 the kinetic energy released during Coulomb explosion is $\text{KER} = \frac{1}{2m_p} (\mathbf{p}_{p1}^2 + \mathbf{p}_{p2}^2)$, where \mathbf{p}_{p1} and \mathbf{p}_{p2} are the proton momenta and m_p is the proton mass. The mapping of internuclear distance $R = \frac{1}{\text{KER}}$ to kinetic energy release is very precise for H_2 [18, 33]. The first ionization event at time t_1 initiates a H_2^+ nuclear wavepacket on the $1s\sigma_g$ ground state. The wavepacket propagates on the light-induced potential energy surfaces and is projected onto the Coulombic potential energy curve by the second ionization event at time $t_2 = t_1 + \Delta t$, see Fig. 1(a). Measuring the momenta of the two protons provides us with the internuclear distance R at which the second ionization step happened. Hence, if the two ionization events are confined to within the first roundtrip of the nuclear wavepacket on the $1s\sigma_g$ potential we can establish a correlation between KER and Δt .

For the experiment we used reaction microscopy [34]. We measured the three-dimensional momentum vectors

of two protons in coincidence with two electrons emerging from the interaction of H_2 molecules with elliptically polarized pulses with a broad spectrum centered around 750 nm (oscillation period $T = 2.5$ fs), a full-width at half maximum (FWHM) duration of 4.5 fs in intensity and a peak intensity of $9 \times 10^{14} \text{ W cm}^{-2}$. The experimental apparatus consists of a two-stage arrangement to provide an internally cold ultrasonic gas jet of hydrogen, and an interaction chamber with an ultra-high vacuum ($1.3 \times 10^{-10} \text{ mbar}$). Electrons and ions were guided by weak magnetic (12 G) and electric (21 V/cm) fields along the spectrometer axis (z -direction) to two position and time sensitive multi-hit detectors. Further details on the reaction microscope can be found in Refs. [3, 35, 36] and on the optical setup in Ref. [11] as well as in Supplemental Material [37].

Fig. 1(c) shows the proton momentum distribution in the laser polarization plane for the double ionization pathway. The anisotropy of the proton distribution indicates the alignment of the polarization ellipse in the laboratory frame. In elliptical light, ionization preferentially takes place twice during the optical cycle [38]. Hence, sequential double ionization in elliptical light occurs with a delay between the two ionization steps of $\Delta t = nT/2; n = 0, 1, 2, \dots$. To calibrate the zero of our time-scale we turn to the KER, shown in Fig. 1(d). For instantaneous double ionization, i.e., $\Delta t = 0$, the H_2

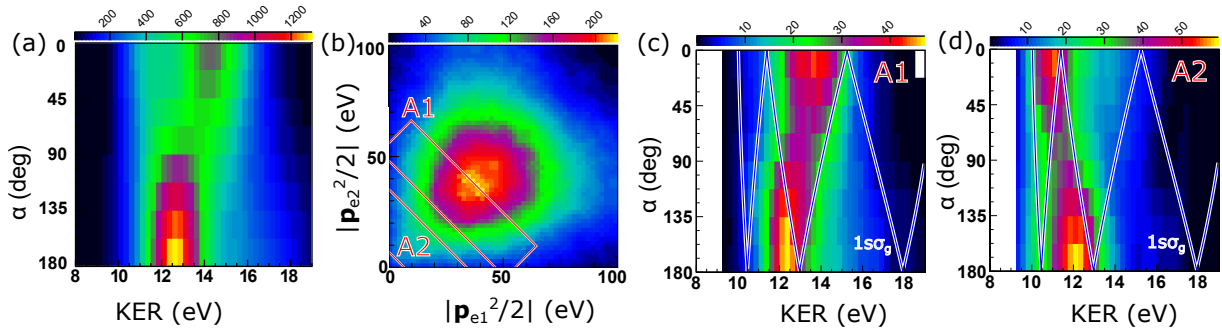


FIG. 2. (a) Double ionization yield as a function of kinetic energy release (KER) and the relative electron emission angle, integrated over the photoelectron energy. (b) Energy distribution of the two emitted photoelectrons (symmetrized about the diagonal). The marked areas $A1$, $A2$ correspond to regions of constant sum energy. Most of the photoelectrons are created with similar energies which indicates that the two-electron emission is symmetrically distributed around the laser pulse peak. (c) Measured fragmentation yield as a function of α and KER obtained when the momenta of the two emitted electrons lie within range $A1$ indicated in (b). (d) Same as (c) but for electron momenta within range $A2$. The thin line in (c) and (d) shows the classical expectation value obtained for vibrational motion on the $1s\sigma_g$ potential energy curve (see text and Supplemental Material [37] for details).

groundstate wavefunction would be projected vertically onto the Coulomb repulsion curve, to yield a KER distribution centered at 19 eV with a FWHM of 2 eV [33]. Thus, based on Fig. 1(d) we can exclude instantaneous double ionization in our experiment.

The observed KER distribution from 10 eV to 18 eV can be related to a timescale, assuming nuclear wavepacket propagation on a given potential energy surface. To this end, we computed the nuclear-stretch motion in between the ionization times t_1 and $t_2 = t_1 + \Delta t$ by solving Newton's equations on the $1s\sigma_g$ energy curve [39]; see Supplemental Material [37] for details on the simulations. The simulation shows that our experiment covers a range of ionization delays starting from about $\Delta t = 0.5T$ (KER ≈ 18 eV) to roughly $\Delta t = 3T$ (KER ≈ 10 eV), with a maximum of the double ionization probability around $\Delta t = 1.5T$ (KER ≈ 13 eV). Smaller Δt -values correspond to smaller internuclear distances, R , where the ionization potential is greatly increased and double ionization probability is accordingly suppressed, see Fig. 1(a). Double ionization delays of $\Delta t \lesssim 0.5T$ require both the increase of the pulse peak intensity and a pulse duration even shorter than the 4.5-fs pulses used here (Supplemental Material [37]).

The energy of each photoelectron, shown in Fig. 1(e), labels the light intensity at the instant of ionization. The peak at 40 eV corresponds to an ionization intensity of about $3.8 \times 10^{14} \text{W/cm}^2$. Therefore, the majority of double ionization events does not occur at the peak of the pulse, in agreement with the prediction of the double ionization delay based on the KER. Sub-cycle sensitivity, finally, is obtained from the relative angle $\alpha = \text{ang}(\mathbf{p}_{e1}, \mathbf{p}_{e2})$ between the two photoelectron momenta \mathbf{p}_{e1} and \mathbf{p}_{e2} , shown in Fig. 1(f). By virtue of the relation $\mathbf{p}_{e1,e2} = -\mathbf{A}(t_{1,2})$ the relative an-

gle $\alpha \in [0^\circ, 180^\circ]$ directly measures Δt within one laser half-cycle. The minimum at $\alpha \approx 90^\circ$ can be attributed to the ellipticity of the pulse. The relative emission angle peaks at $\alpha = 180^\circ$, thus indicating a preferential double ionization at a delay of half-integer optical cycles, consistent with the $\Delta t = 1.5T$ deduced from the maximum of the KER distribution.

However, the estimates based on the isolated observables in Fig. 1(d-f) do not yield a true sub-cycle resolution of the coupled electronic and nuclear dynamics. To obtain this, we will in the following examine the relation between KER, photoelectron emission angle and energy to demonstrate how the sub-cycle dynamics of the nuclear wavepacket can be accessed by correlating these three observables. In Fig. 2(a) we show the correlation between the two main hands of the molecular clock: the relative emission angle α of the photoelectrons and the KER of the protons. A previously indistinguishable maximum in the double ion yield at a KER of 14.5 eV is associated with a relative emission angle of zero degrees, i.e., the parallel emission of the two photoelectrons. The main maximum at a KER of 12.6 eV is slightly lower than in Fig. 1(d) and associated with anti-parallel electron emission. Finally, a third peak at a KER of 11.5 eV and parallel emission is weakly distinguishable.

Thus, by correlating α with KER, we obtain a powerful parametric framework for representing the coupled electron and nuclear dynamics taking place in between the two ionization steps. For example, if the $2p\sigma_u$ energy level is populated by shake-up during the first ionization step or also at later times by resonant transitions, the corresponding parametric curves in the α -KER frame of reference will look distinctively different from the one corresponding to vibrational motion on the $1s\sigma_g$ level; see Supplemental Material [37] for a comparison of curves ob-

tained for different scenarios. Therefore, the ionization-fragmentation dynamics can be studied by comparison of the measured fragmentation yield to a simulated curve for a given scenario, e.g., for motion only on the $1s\sigma_g$ energy level.

Further insight into the molecular dynamics within the duration of the pulse can be obtained when the magnitudes of the photoelectron momenta $|\mathbf{p}_{e1,e2}|$ are analyzed. $|\mathbf{p}_{e1,e2}|$ provide an additional time reference linked to the fast rise time of a few-cycle pulse's envelope [10]. Gating on $|\mathbf{p}_{e1,e2}|$, thus allows selecting a range of ionization delays Δt . As a result, it becomes possible to obtain sub-cycle traces of the molecular dynamics for certain ranges of delays Δt in the two-electron emission and, moreover, as we will show further below, even attosecond snapshots of the propagating vibrational wavepacket.

For the purpose of the following analysis we show the energies of both photoelectrons in Fig. 2(b). The highest double ionization probability is found for similar momenta of both electrons. Hence, the highest double ionization yield is from events where both electrons are emitted symmetrically around the peak of the pulse envelope. For example, the region *A1* indicated in the correlated energy spectrum Fig. 2(b) corresponds to situations where both electrons are emitted within $\Delta t = 1.2T - 1.7T$. Region *A2* at smaller energies corresponds to emissions with longer delay, $\Delta t = 2.3T - 3.2T$.

The capabilities opened up by the selection of the emission time-window based on $|\mathbf{p}_{e1,e2}^2/2|$ are demonstrated in Figs. 2(c,d). In these figures we show the measured distribution of the fragmentation yield in the α -KER plane for the two regions of electron energies *A1* and *A2* in Fig. 2(b). Accordingly, the corresponding ranges of the yield distribution in the α -KER plane in Figs. 2(c) and (d) show the vibrational wavepacket evolution approximately in the time ranges of $1.2T - 1.7T$ and $2.3T - 3.2T$ after the first ionization step, respectively. A movie obtained for arbitrary selections of $|\mathbf{p}_{e1,e2}|$ is available as Supplemental Material [37]. The measured distributions in Figs. 2(c,d) are compared to the simulated curve obtained for wavepacket motion on the $1s\sigma_g$ energy level (described in Supplemental Material [37]). The measured distributions show no signs of shake-up excitation that would appear for $\text{KER} > 19$ eV. Likewise, they show negligible yield in the range $\text{KER} < 10$ eV that corresponds to resonant excitation to the $2p\sigma_u$ energy curve. Overall, the measured distributions agree well with the simulated curve for nuclear motion on the $1s\sigma_g$ curve, although there are some small deviations visible for the smaller emission delays Δt , cf. Fig. 2(c).

As $\alpha = 0 - 180^\circ$ corresponds to one laser half cycle, by limiting α to small intervals, attosecond snapshots of the KER distribution can be extracted from these traces. By virtue of the Coulomb law, $\text{KER} = 1/R$ can be converted to internuclear distance R . Thus, it becomes possible to obtain snapshots of the absolute value of the

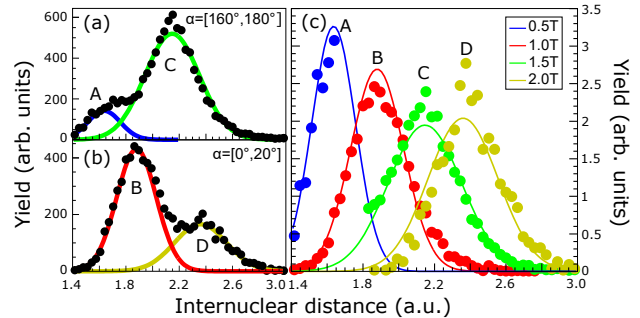


FIG. 3. Measured fragmentation yield (dots) over R for ionization events separated by an even (a) and odd (b) number of half cycles. (a) The distributions result from the selection $\alpha = [160^\circ, 180^\circ]$, corresponding to ionization events taking place within a range of ± 70 as around $\Delta t = 2n\frac{T}{2}$, $n = 0, 1, 2$. (b) Same as (a) but for $\alpha = [0^\circ, 20^\circ]$, corresponding to ± 70 as around $\Delta t = (2n + 1)\frac{T}{2}$, $n = 0, 1, 2$. The colored lines labeled A-D are Gaussian fits to the data. The labels A-D correspond with those in Fig. 1. (c) Measured fragmentation yield (dots) from (a,b) but with additional restrictions on the magnitude of the electron momentum (see Supplemental Material [37] for details) in comparison with the Gaussian fits from (a,b). The areas of the distributions A-D were normalized to one.

vibrational wavepacket, $|\chi(R, \Delta t)|^2$, for very short time-intervals around certain values of Δt .

To obtain $|\chi|^2$ we select slices in the α -KER distribution for $\alpha = [0^\circ, 20^\circ]$ and $\alpha = [160^\circ, 180^\circ]$ corresponding to intervals of Δt of about 140 as. The yield distributions obtained by these selections are plotted in Fig. 3(a,b) as a function of R together with Gaussian fits. The Gaussian fits agree well with yield distributions obtained by more sophisticated selections (detailed in Supplemental Material [37]) that also involve gating on $|\mathbf{p}_{e1,e2}|$ as described above, see Fig. 3(c). The four distributions in Fig. 3(c) constitute snapshots of $|\chi(R, \Delta t)|^2$ with an uncertainty of about ± 70 as around $\Delta t = 0.5T, 1T, 1.5T, 2T$ and with a spatial resolution of about 0.02 a.u. (about 1 pm).

The equilibrium internuclear distance of H_2 is 1.4 a.u. Fig. 3(c) shows that after half a laser cycle ($\Delta t = 1.25$ fs) the H_2^+ nuclear wavepacket has propagated in distance by about 0.2 a.u. For larger values of Δt , our measurement reveals how the wavepacket progressively moves to larger internuclear distances and spreads in space. Compared with previous experiments that probed the nuclear motion of H_2^+ after strong-field laser ionization [18], our measurement is, to the best of our knowledge, the first one to reveal not only the position but also the shape of the wavepacket. Additionally, our measurement probes the wavepacket on a finer grid of Δt and with significantly higher temporal resolution (i.e., uncertainty in Δt).

In conclusion, we introduced a new method, that allows tracing molecular dynamics on sub-femtosecond times *during* strong-field interaction following field-ionization. The method exploits the rotation of the elec-

tric field vector of elliptically polarized light as an attosecond temporal reference, and the dependence of the ion fragment energy on the molecular geometry as a clock for nuclear motion. Although demonstrated here for H_2 , for which the nuclear clock shows a $1/R$ dependence, this is not a pre-requisite of the method; any monotonic dependence of fragment energy on nuclear geometry is suitable. We therefore expect a wide applicability of the presented method and envision that it can also be applied to reasonably fast dissociative few-particle fragmentation channels in polyatomic molecules, as many of them fulfill this requirement. We highlight the high temporal resolution and spatial sensitivity of the method by demonstrating tracing of the vibrational wavepacket evolution in H_2^+ with a temporal uncertainty of about ± 70 as and a spatial resolution of about 1 pm. The resolution of this technique can be expected to be further improved by exploitation of the carrier-envelope phase of few-cycle laser pulses [11].

This work was financed by the Austrian Science Fund (FWF), Grants No. P28475-N27, and P30465-N27.

* vaclav.hanus@tuwien.ac.at

† andre.staudte@nrc-cnrc.gc.ca

‡ markus.kitzler@tuwien.ac.at

- [1] M. F. Kling, P. von den Hoff, I. Znakovskaya, and R. de Vivie-Riedle, *Phys. Chem. Chem. Phys.* **15**, 9448 (2013).
- [2] A. S. Alnaser and I. V. Litvinyuk, *J. Phys. B At. Mol. Opt. Phys.* **50**, 032002 (2017).
- [3] X. Xie, K. Doblhoff-Dier, S. Roither, M. S. Schöffler, D. Kartashov, H. Xu, T. Rathje, G. G. Paulus, A. Baltuška, S. Gräfe, and M. Kitzler, *Phys. Rev. Lett.* **109**, 243001 (2012), [arXiv:1208.4545](https://arxiv.org/abs/1208.4545).
- [4] X. Xie, S. Roither, M. Schöffler, E. Lötstedt, D. Kartashov, L. Zhang, G. G. Paulus, A. Iwasaki, A. Baltuška, K. Yamanouchi, and M. Kitzler, *Phys. Rev. X* **4**, 021005 (2014).
- [5] X. Xie, E. Lötstedt, S. Roither, M. Schöffler, D. Kartashov, K. Midorikawa, A. Baltuška, K. Yamanouchi, and M. Kitzler, *Sci. Rep.* **5**, 12877 (2015).
- [6] T. Ergler, A. Rudenko, B. Feuerstein, K. Zrost, C. Schröter, R. Moshhammer, and J. Ullrich, *Phys. Rev. Lett.* **97**, 193001 (2006).
- [7] H. Xu, F. He, D. Kielpinski, R. T. Sang, and I. V. Litvinyuk, *Sci. Rep.* **5**, 1 (2015), [arXiv:1504.04676](https://arxiv.org/abs/1504.04676).
- [8] C. Maharjan, A. Alnaser, X. Tong, B. Ulrich, P. Ranitovic, S. Ghimire, Z. Chang, I. Litvinyuk, and C. Cocke, *Phys. Rev. A* **72**, 041403 (2005).
- [9] P. Eckle, M. Smolarski, P. Schlup, J. Biegert, A. Staudte, M. Schöffler, H. G. Muller, R. Dörner, and U. Keller, *Nat. Phys.* **4**, 565 (2008).
- [10] A. N. Pfeiffer, C. Cirelli, M. Smolarski, R. Dörner, and U. Keller, *Nat. Phys.* **7**, 428 (2011).
- [11] M. S. Schöffler, X. Xie, P. Wustelt, M. Möller, S. Roither, D. Kartashov, A. M. Sayler, A. Baltuska, G. G. Paulus, and M. Kitzler, *Phys. Rev. A* **93**, 063421 (2016).
- [12] P. Wustelt, M. Möller, M. S. Schöffler, X. Xie, V. Hanus, A. M. Sayler, A. Baltuska, G. G. Paulus, and M. Kitzler, *Phys. Rev. A* **95**, 023411 (2017).
- [13] J. Wu, M. Meckel, L. P. H. Schmidt, M. Kunitski, S. Voss, H. Sann, H. Kim, T. Jahnke, A. Czasch, and R. Dörner, *Nat. Commun.* **3**, 1113 (2012).
- [14] J. Wu, L. Schmidt, M. Kunitski, M. Meckel, S. Voss, H. Sann, H. Kim, T. Jahnke, A. Czasch, and R. Dörner, *Phys. Rev. Lett.* **108**, 183001 (2012).
- [15] J. Wu, M. Magrakvelidze, L. P. H. Schmidt, M. Kunitski, T. Pfeifer, M. Schöffler, M. Pitzer, M. Richter, S. Voss, H. Sann, H. Kim, J. Lower, T. Jahnke, A. Czasch, U. Thumm, and R. Dörner, *Nat. Commun.* **4**, 2177 (2013).
- [16] X. Gong, Q. Song, Q. Ji, H. Pan, J. Ding, J. Wu, and H. Zeng, *Phys. Rev. Lett.* **112**, 243001 (2014).
- [17] H. Stapelfeldt, E. Constant, H. Sakai, and P. Corkum, *Phys. Rev. A* **58**, 426 (1998).
- [18] H. Niikura, F. Légaré, R. Hasbani, M. Y. Ivanov, D. M. Villeneuve, and P. B. Corkum, *Nature* **421**, 826 (2003).
- [19] F. Légaré, I. Litvinyuk, P. Dooley, F. Quéré, A. Bandrauk, D. Villeneuve, and P. Corkum, *Phys. Rev. Lett.* **91**, 093002 (2003).
- [20] F. Légaré, K. Lee, I. Litvinyuk, P. Dooley, A. Bandrauk, D. Villeneuve, and P. Corkum, *Phys. Rev. A* **72**, 052717 (2005).
- [21] S. Erattupuzha, C. L. Covington, A. Russakoff, E. Lötstedt, S. Larimian, V. Hanus, S. Bubin, M. Koch, S. Gräfe, A. Baltuška, X. Xie, K. Yamanouchi, K. Varga, and M. Kitzler, *J. Phys. B At. Mol. Opt. Phys.* **50**, 125601 (2017).
- [22] A. Staudte, *Subfemtosecond Electron Dynamics of H2 in Strong Fields or The Quest for the Molecular Clock*, Dissertation, Johann Wolfgang Goethe Universität Frankfurt am Main (2005).
- [23] H. Ibrahim, C. Lefebvre, A. D. Bandrauk, A. Staudte, and F. Légaré, *J. Phys. B At. Mol. Opt. Phys.* **51**, 042002 (2018).
- [24] H. Niikura, F. Légaré, R. Hasbani, A. D. Bandrauk, M. Y. Ivanov, D. M. Villeneuve, and P. B. Corkum, *Nature* **417**, 917 (2002).
- [25] X. Urbain, B. Fabre, E. Staicu-Casagrande, N. de Ruette, V. Andrianarijaona, J. Jureta, J. Posthumus, A. Saenz, E. Baldit, and C. Cornaggia, *Phys. Rev. Lett.* **92**, 163004 (2004).
- [26] I. Litvinyuk, F. Légaré, P. Dooley, D. Villeneuve, P. Corkum, J. Zanghellini, A. Pegarkov, C. Fabian, and T. Brabec, *Phys. Rev. Lett.* **94**, 033003 (2005).
- [27] M. Haertelt, X.-B. Bian, M. Spanner, A. Staudte, and P. B. Corkum, *Phys. Rev. Lett.* **116**, 133001 (2016).
- [28] F. Faisal, *J. Phys. B At. Mol.* **6**, L89 (1973).
- [29] H. Reiss, *Phys. Rev. A* **22**, 1786 (1980).
- [30] Z. Vager, R. Naaman, and E. P. Kanter, *Science* **244**, 426 (1989).
- [31] S. Chelkowski, P. Corkum, and A. Bandrauk, *Phys. Rev. Lett.* **82**, 3416 (1999).
- [32] H. Katsuki, H. Chiba, B. Girard, C. Meier, and K. Ohmori, *Science* **311**, 1589 (2006).
- [33] T. Weber, A. O. Czasch, O. Jagutzki, A. K. Müller, V. Mergel, A. Kheifets, E. Rotenberg, G. Meigs, M. H. Prior, S. Daveau, A. Landers, C. L. Cocke, T. Osipov, R. Díez Muiño, H. Schmidt-Böcking, and R. Dörner, *Nature* **431**, 437 (2004).
- [34] R. Dörner, V. Mergel, O. Jagutzki, L. Spielberger, J. Ull-

- rich, R. Moshhammer, and H. Schmidt-Böcking, *Phys. Rep.* **330**, 95 (2000).
- [35] L. Zhang, X. Xie, S. Roither, D. Kartashov, Y. Wang, C. Wang, M. Schöffler, D. Shafir, P. B. Corkum, A. Baltuška, I. Ivanov, A. Kheifets, X. Liu, A. Staudte, and M. Kitzler, *Phys. Rev. A* **90**, 061401 (2014), [arXiv:1404.5742](#).
- [36] X. Xie, T. Wang, S. Yu, X. Lai, S. Roither, D. Kartashov, A. Baltuška, X. Liu, A. Staudte, and M. Kitzler, *Phys. Rev. Lett.* **119**, 243201 (2017), [arXiv:1707.07636](#).
- [37] See Supplemental Material at LINK (will be inserted by publisher) for details of the experiment and data interpretation.
- [38] P. Eckle, A. N. Pfeiffer, C. Cirelli, A. Staudte, R. Dörner, H. G. Muller, M. Büttiker, and U. Keller, *Science* **322**, 1525 (2008).
- [39] T. Sharp, *At. Data Nucl. Data Tables* **2**, 119 (1970).

Sub-femtosecond tracing of molecular dynamics during strong-field interaction

Supplemental Material

Václav Hanus, Sarayoo Kangaparambil, Seyedreza Larimian, Martin Dörner-Kirchner, Xinhua Xie, Markus S. Schöffler, Gerhard G. Paulus, Andrius Baltuška, André Staudte, Markus Kitzler-Zeiler

1 Experimental details

Peak intensity and ellipticity were calibrated by analyzing the electron momentum distribution obtained for single ionization of helium with the same pulse as in the experiment on H_2 , using the method described in Ref. 1-SM. By this approach we obtained the laser intensity in the interaction region as $9 \times 10^{14} \text{ W cm}^{-2}$. The ellipticity, defined as the ratio of the electric field strengths perpendicular and parallel to the main axis of the polarization ellipse, E_{\perp}/E_{\parallel} was 0.85. The direction of the polarization ellipse was determined from the angular distribution of protons emitted by Coulomb explosion of doubly charged hydrogen, H_2^{2+} . The rotation of the molecule during the ionization and Coulomb explosion processes was neglected given the short pulse duration used in the experiment. To minimize smearing of the laser intensity along the propagation direction of the laser beam (coordinate x), the gas jet (propagating along y) was cut by adjustable razor blades to about $10 \mu\text{m}$, much shorter than the Rayleigh length of the laser beam ($\approx 200 \mu\text{m}$). The duration of the pulses ($\approx 4.5 \text{ fs}$) and their CEP-values (not analyzed in the present work) were obtained with a phase-meter device.^{2-SM}

In our experiments we use a reaction microscope to measure the momentum vectors of the two electrons, $\mathbf{p}_{e1,e2}$ and two protons $\mathbf{p}_{p1,p2}$ ejected during fragmentation of doubly charged hydrogen, H_2^{2+} . In some cases the dead time of the detectors inhibits the detection of both electrons and only one electron is detected. In these cases we calculated the momentum of the missed electron by exploiting momentum conservation between the momentum of the other electron and the ions, $\mathbf{p}_{e2} = -(\mathbf{p}_{p1} + \mathbf{p}_{p2} + \mathbf{p}_{e1})$. The kinetic energy released during the Coulomb explosion of the two protons after double ionization is given by $\text{KER} = \frac{1}{2m_p} (\mathbf{p}_{p1}^2 + \mathbf{p}_{p2}^2)$, with m_p being the proton mass (≈ 1836 in atomic units). The measured distribution of KER is shown in Fig. 1-SM(a). From the electron momentum vectors we calculate the emission angle α between the two electrons using the scalar product, $\cos(\alpha) = \frac{\mathbf{p}_{e1}\mathbf{p}_{e2}}{|\mathbf{p}_{e1}||\mathbf{p}_{e2}|}$. Since the experiment is not able to distinguish between the first emitted and second emitted electron, the angle ranges from 0° to 180° . The measured proton yield as a function of KER and α before applying any conditions on electron energy is shown in Fig. 1-SM(b).

2 Electronic and nuclear dynamics in the KER- α representation

As discussed in the main manuscript, the measured fragmentation yield as a function of KER and α constitutes a powerful representation for depicting the coupled electron and nuclear motion taking place during the two ionization steps. In Fig. 2 of the main manuscript we compare the measured distribution to its simulated classical expectation value for the case of vibrational motion taking place only on the $1s\sigma_g$ energy level. Here we provide details on these simulations and will furthermore show how the classical parametric curves look for different fragmentation pathways.

Fig. 2-SM shows examples for these curves for three different fragmentation pathways. To calculate the parametric curves in Fig. 2-SM we solve Newton's equations on the $1s\sigma_g$ and $2p\sigma_u$ potential energy curves given in Ref. 3-SM. We assume that upon the first ionization step at the instant t_1 the $1s\sigma_g$ curve

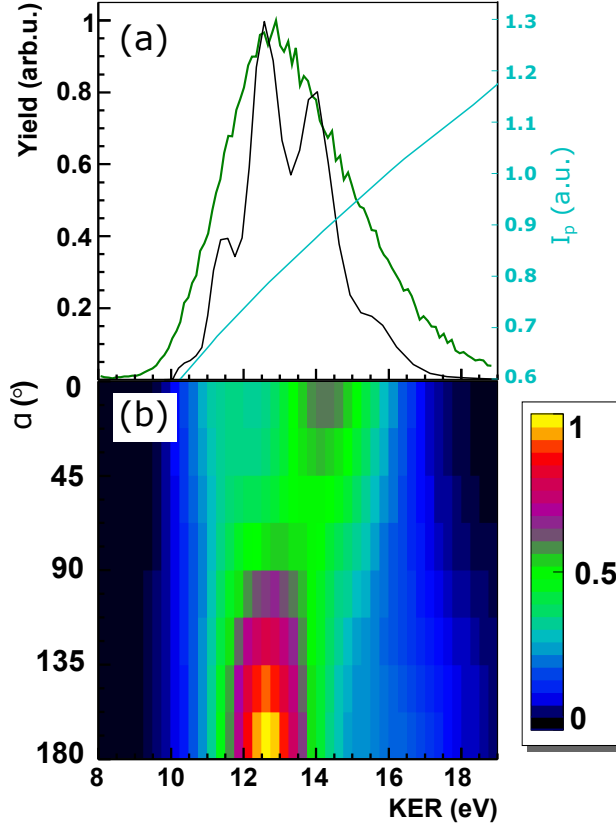


Figure 1-SM: (a) Measured distribution of the KER (green) in comparison with simulated data (black). The light blue line (ordinate on the right applies) depicts the dependence of the ionization potential on KER used in the simulation. See Sec. 3 for details. (b) The measured KER distribution from (a) resolved in the relative emission angle of the two electrons, α .

of H_2^+ is populated at an internuclear distance R given by the equilibrium distance of H_2 . We further assume that the potential energy curve is unaffected by the laser electric field and that the nuclear motion is determined purely by the gradient of the populated potential energy curve ($1s\sigma_g$ or $2p\sigma_u$) at any given internuclear distance. Transitions due to absorption of photons between the $1s\sigma_g$ and $2p\sigma_u$ curves after the first ionization step are modeled as vertical transitions. They can take place when the energies of the two levels $E_{2p\sigma_u}(R)$ and $E_{1s\sigma_g}(R)$ become resonant with n photons, $E_{2p\sigma_u}(R) - E_{1s\sigma_g}(R) = n\hbar\omega$, or due to shake-up. The second ionization step takes place at an instant $t_2 = t_1 + \Delta t$. At t_2 the repulsive Coulomb curve is populated and the KER (in atomic units) is calculated as $\text{KER} = \frac{1}{R} + E_K$, with E_K the kinetic energies of the protons at time t_2 . Depending on the pathway of the fragmentation dynamics along the $1s\sigma_g$ and $2p\sigma_u$ potential energy curves, the sequence of transitions between these two curves and the ionization delay Δt , the resulting KER- α parametric curves look distinctively different. Their shape, thus, is characteristic for the nuclear and electronic dynamics taking place during the time Δt . Comparison of the measured fragmentation yield resolved in the two-dimensional coordinate system KER vs. α to simulated curves, thus, allows identifying the molecular motion taking place during the interaction with the laser field.

The blue line in Fig. 2-SM(a) corresponds to the case, where vibrational motion taking place in between the two ionization steps at times t_1 and $t_2 = t_1 + \Delta t$, respectively, occurs exclusively on the $1s\sigma_g$ energy level. The first ionization step starts the nuclear motion on the $1s\sigma_g$ curve. If the second ionization step would occur immediately after the first one, $\Delta t \rightarrow 0$, the angle α between the momentum vectors of the two emitted electrons would be zero and one would measure a KER value indicated by the vertical

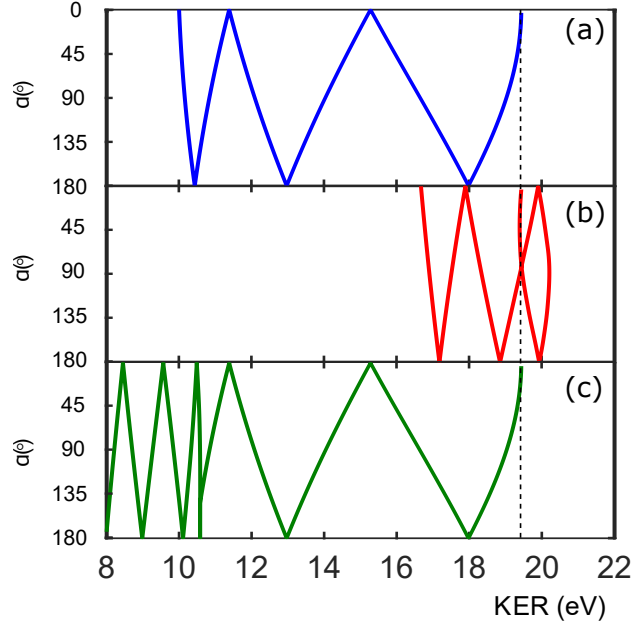


Figure 2-SM: Classically calculated connection between the relative electron angle α and KER for selected fragmentation pathways. See text for details of the calculations. (a) The nuclear wavepacket propagates on the $1s\sigma_g$ state starting from the equilibrium internuclear distance of H_2 . (b) Shakeup of the molecular ion to the $2p\sigma_u$ state immediately after the first ionization step. (c) Propagation on the $1s\sigma_g$ state until the internuclear distance 2.6 a.u. where the $1s\sigma_g$ and $2p\sigma_u$ states become resonant via a five photon transition and a transition to the $2p\sigma_u$ level is made. The dashed vertical line indicates the KER value corresponding to the equilibrium distance of H_2 (1.4 a.u.).

dashed line in Fig. 2-SM(a) (larger than 19 eV). As Δt increases, the nuclear motion proceeds on the $1s\sigma_g$ level and the internuclear distance increases, resulting in decreasing KER. If the second ionization step would take place half a cycle after the first one, i.e., at $\Delta t = \pi/\omega$, with ω the laser oscillation frequency, the angle between the two electron momentum vectors would be 180° and KER would amount to roughly 18 eV. For $\pi/\omega < \Delta t < 2\pi/\omega$ the angle α decreases again towards zero and KER decreases further due to the ongoing nuclear stretch motion, until at $\Delta t = 2\pi/\omega$ the emission direction of the second electron equals that of the first one and the angle α becomes zero again. The nuclear stretch motion and the concomitant decrease of KER persist during the next two laser cycles. About three laser cycles after the first ionization step, at $\Delta t \approx 6\pi/\omega$ and $\alpha \approx 0$, the maximum classically allowed value of the internuclear distance R for the assumed initial potential energy (dictated by the vertical transition to the $1s\sigma_g$ curve at $R = 1.4$ a.u.) is reached. From there on, the internuclear distance decreases again and the blue curve in Fig. 2-SM(a) is traversed in the direction towards increasing KER.

The curve in Fig. 2-SM(b) corresponds to molecular dynamics where a shake-up process in the molecular ion to the $2p\sigma_u$ state immediately after the first ionization step takes place. From there on the vibrational wavepacket proceeds on the dissociative $2p\sigma_u$ energy curve. The molecule starts to dissociate and the internuclear distance R quickly increases. As the $2p\sigma_u$ curve initially shows a steeper dependence on R as the Coulomb curve, KER values higher than those obtained for sequential ionization with $\Delta t \rightarrow 0$ are obtained, as long as the second ionization step takes place within about the first laser cycle after the first one. Dissociation is completed within a delay Δt corresponding to about three laser cycles. After this delay the internuclear distance has grown to such large values that the KER does not significantly decrease anymore for longer delays.

Fig. 2-SM(c), finally, shows a fragmentation scenario, where nuclear motion first proceeds on the $1s\sigma_g$ energy curve, until at the internuclear distance 2.6 a.u., where the $1s\sigma_g$ and $2p\sigma_u$ states become resonant

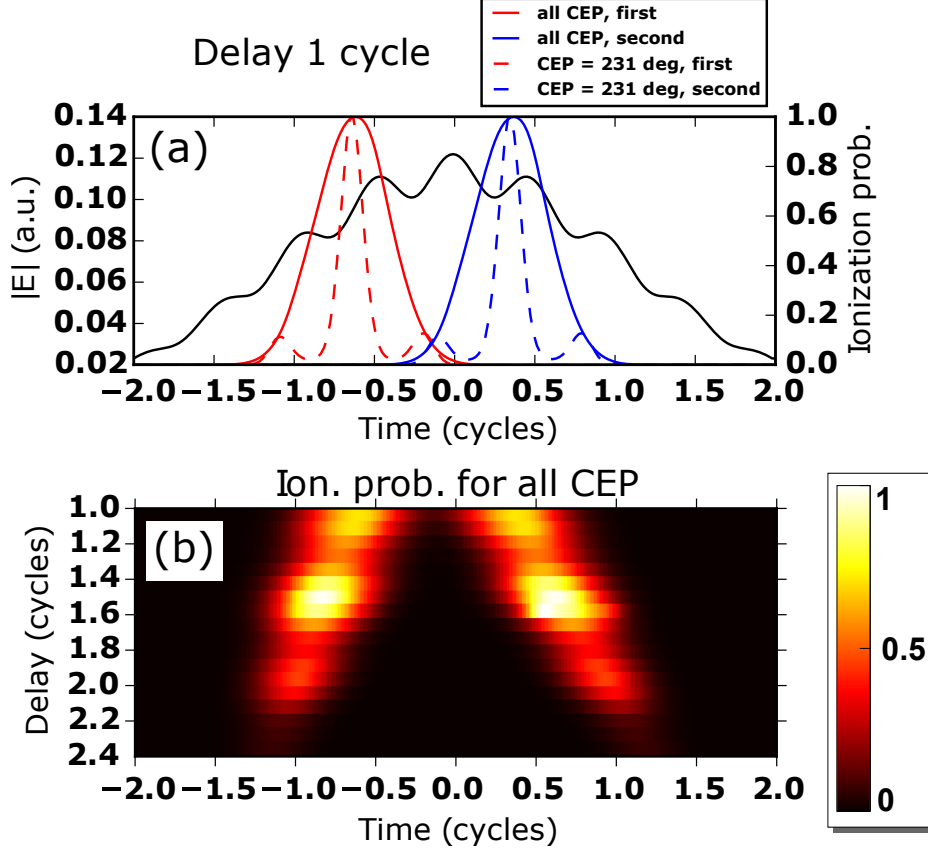


Figure 3-SM: (a) Ionization rates of the first (dashed red) and second (dashed blue) ionization step for the laser electric field shown in black. The corresponding full lines are obtained when one averages over all values of the CEP. (b) CEP-averaged ionization rates for the first (left branch) and second (right branch) emission event as a function of delay between the two events. All rates are normalized to one at their maximum values.

via a five photon transition, a transition to the $2p\sigma_u$ level takes place (around KER= 10.3 eV). From this point on, the nuclear motion takes place on the $2p\sigma_u$ energy curve and the molecule dissociates. As the gradient of the $2p\sigma_u$ energy curve is already quite small at and beyond the R -value where the transition happens, the nuclear stretch motion is slow and KER decreases only relatively little per laser cycle.

3 Selection of ionization delay by gating on electron momentum

We discuss in the main manuscript that gating on the electrons' energy can be used to select the range of relative delays between the two ionization steps, Δt , see Fig. 2 and the corresponding text in the main manuscript. Here, we provide the results of simulations to visualize this capability.

In these simulations we model the double ionization and nuclear dynamics using (semi-)classical models for a laser electric field of the form

$$\mathbf{E}(t) = E_{\parallel} \cos(\omega t + \varphi) + E_{\perp} \sin(\omega t + \varphi), \quad (1)$$

where E_{\parallel} and $E_{\perp} = \varepsilon E_{\parallel}$ denote the peak electric field strengths along the major respectively minor polarization ellipse, ε is the ellipticity, and φ is the carrier-envelope phase (CEP). For a comparison with

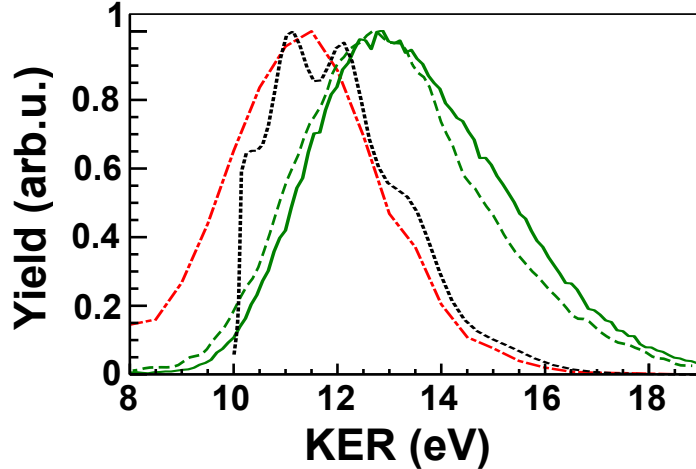


Figure 4-SM: The full respectively dashed green lines show measured KER distributions of doubly ionized H_2 for peak intensities $9 \times 10^{14} \text{ W/cm}^2$ and $1.2 \times 10^{15} \text{ W/cm}^2$ for a pulse duration of $\approx 4.5 \text{ fs}$. The dashed-dotted red KER distribution is obtained for a 5.5-fs pulse with a peak intensity of $1.7 \times 10^{15} \text{ W/cm}^2$. The dotted black KER distribution is obtained by simulations as described in Section 3 for the pulse parameters corresponding to the measured dashed-dotted red distribution.

the experiments, where the influence of the CEP is not considered, we repeat the simulations for different values of $\varphi \in [0, 2\pi]$ and subsequently average over φ . The dependence of the laser electric field along the laser propagation direction (perpendicular to the \parallel and \perp directions) is neglected based on the thin jet used in the experiments (see Section 1).

Ionization is modeled as described in Ref. 4-SM using an ADK-type formula. For the first ionization step, taking place at time t_1 , the value of the ionization potential is $I_{p,1} = 15.4 \text{ eV}$.^{5-SM} The molecules are assumed to be randomly oriented in space and the angular dependence of the ionization potential is neglected. Ionization-depletion of the states is properly accounted for.^{4-SM} The first ionization step triggers nuclear motion in the cation H_2^+ . This nuclear motion is modeled classically as described in Section 2. The second ionization step happens Δt after the first ionization step at time $t_2 = t_1 + \Delta t$, when the two nuclei have reached a certain internuclear distance, R . The ionization potential for the second ionization step, $I_{p,2}(R)$, depends on R . $I_{p,2}(R)$ decreases monotonically with R and could for example be determined by the energetic difference between the Coulomb explosion curve $1/R$ and the active molecular potential curve. We use the $I_{p,2}(R)$ curve as a parameter and adjust its offset and linear slope to obtain good agreement with the measured KER distribution. See the Fig. 1-SM(a) for a comparison of the calculated and measured KER distributions and the corresponding $I_{p,2}(R)$ curve. To obtain a KER distribution from our simulations we loop over the times t_1 and $t_2 > t_1$ and calculate the double ionization probability $P = p_1 p_2$, where p_1 respectively p_2 denote the single and double ionization probabilities for this combination of t_1 and t_2 .^{4-SM} The corresponding KER value is given by $\text{KER} = 1/R$. By summing up all combinations of t_1 and $t_2 > t_1$ with their respective double ionization probability P we obtain distributions such as the one shown in Fig. 1-SM(a).

This model can be used to visualize the dependence between the two electrons' momenta $\mathbf{p}_{e1,e2}$ and the ionization delay Δt that we exploit for obtaining Figs. 2(c) and 2(d) in the main manuscript. Fig. 3-SM shows the ionization probability predicted by the model for different values of Δt , when the nuclear motion in between the two ionization steps takes place on the $1s\sigma_g$ energy curve. Because the internuclear distance R increases monotonically with Δt , the ionization potential for the second ionization step, $I_{p,2}(R)$, decreases with increasing R . To overcome the high ionization potential at small internuclear distances, the second ionization step at t_2 needs to happen as close as possible to the peak of the laser pulse where the electric field strength is highest. As a consequence, for small ionization delays Δt (i.e., for small R), the ionization events will happen close to the pulse peak. Indeed, Fig. 3-SM shows that for small

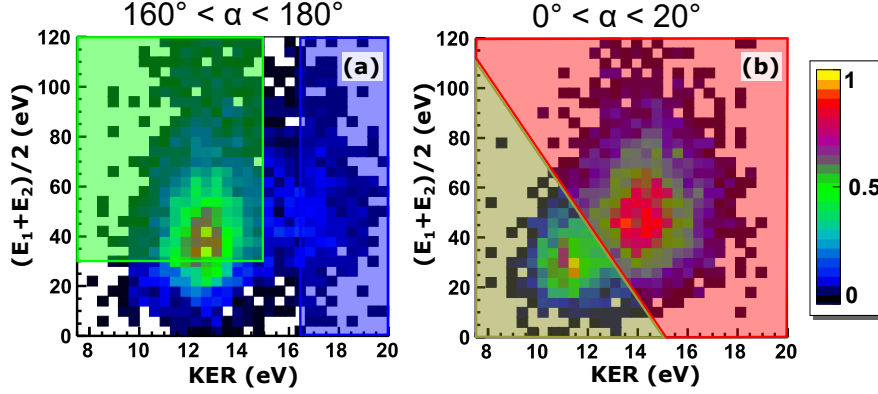


Figure 5-SM: Measured distributions of the fragmentation yield as a function of KER and the averaged sum of the energy of the two emitted electrons for two ranges of the angle between the two electron momentum vectors α as indicated above the figures. The colored boxes visualize the selections from which the shapes of the vibrational wavepacket shown in Fig. 3 in the main manuscript is obtained by integration over the boxes. The colors blue, red, green and yellow correspond to the ionization delays $\Delta t = 0.5T, 1.0T, 1.5T, 2.0T$, with $T = 2\pi/\omega$ the laser cycle duration.

delays the two emission events take place approximately symmetrically about the peak of the pulse, whereas for larger delays (larger R), the instants of ionization t_1 and t_2 shift symmetrically away from the pulse peak. The momenta of the two emitted electrons are given by $\mathbf{p}_{ei} = -\mathbf{A}(t_i)$, $i = 1, 2$ with $\mathbf{A}(t) = -\int_{-\infty}^t \mathbf{E}(t') dt'$ derived from the laser electric field defined in Equ. (1). Thus, larger values of $\mathbf{p}_{e1,e2}$ are obtained for ionization times t_1 and t_2 close to the pulse peak. As a consequence, gating on the electrons' momenta, allows selecting the ionization delay Δt , cf. Fig. 3-SM.

4 Role of pulse duration in the molecular clock

We show in Fig. 2 of the main manuscript and in the corresponding text that for the pulse parameters used in our experiment the useful range of Δt is about 0.5 to $3T$, with $T = 2\pi/\omega$ the duration of the laser cycle. Smaller delays are suppressed due to the very large ionization potential for small internuclear distances, cf. the sketch in Fig. 1(a) of the main manuscript. For obtaining larger delays (smaller KER values), our pulses are too short. One could think that by simply increasing the laser intensity it would be possible to enhance the ionization yield at shorter internuclear distances, thereby accessing smaller values of Δt . However, this is not the case since higher intensity would not only enhance ionization around the pulse peak (where Δt is small), but also at the rising and falling wings of the pulse envelope (corresponding to large values of Δt). Measurements for different peak intensity (but equal pulse duration) indeed show that the width of the KER distribution depends only marginally on intensity, compare the green curves in Fig. 4-SM.

In contrast, the KER distribution depends very sensitively on the duration of the pulse. An increase of only 1 fs to 5.5 fs results in a strong shift of the KER distribution to lower KER and therewith to larger values of Δt , as shown in Fig. 4-SM by the measured (red) and simulated (black) KER distributions, where the simulated KER distribution is obtained by the procedure described in Section 3. This high sensitivity is understandable, as the ionization potential for the second ionization step, $\text{H}_2^+ \rightarrow \text{H}_2^{2+}$, rapidly decreases with R , see the sketch in Fig. 1(a) of the main manuscript. As a consequence, longer delays between the two ionization steps, i.e., larger Δt , are energetically preferred and will inevitably take place if they are accommodated by the pulse duration. Short delays (small Δt , high KER-values), in contrast, need to be enforced by squeezing the two ionization events into the short time-window of short pulses. Accessing Δt -values below $0.5T$ would necessitate intense pulses still shorter than 4.5 fs used in the experiment described in the main manuscript.

5 Retrieval of the vibrational wavepacket in H_2^+

We show in Fig. 3 of the main manuscript that the vibrational wavepacket in H_2^+ launched during the first ionization step can be retrieved from measured data at certain instants during the pulse. As described in the text corresponding to that figure, the quality of the retrieval can be improved by careful choices of the ranges of KER, α and the absolute value of electron momentum respectively electron energy. Fig. 5-SM visualizes the selection ranges that were used for the retrieval shown in Fig. 3 of the main manuscript.

References

- 1-SM Smeenk, C. *et al.* Precise in-situ measurement of laser pulse intensity using strong field ionization. *Opt. Express* **19**, 9336 (2011).
- 2-SM Saylor, A. M. *et al.* Precise, real-time, every-single-shot, carrier-envelope phase measurement of ultrashort laser pulses. *Opt. Lett.* **36**, 1 (2011).
- 3-SM Sharp, T. Potential-energy curves for molecular hydrogen and its ions. *At. Data Nucl. Data Tables* **2**, 119–169 (1970).
- 4-SM Tong, X. M. & Lin, C. D. Time-resolved sequential double ionization of D_2 molecules in an intense few-cycle laser pulse. *Phys. Rev. A* **70**, 023406 (2004).
- 5-SM Dibeler, V. H., Reese, R. M. & Krauss, M. Mass-Spectrometric Study of Photoionization. II. H_2 , HD, and D_2 . *J. Chem. Phys.* **42**, 2045–2048 (1965).